RESEARCH ARTICLE

Comparison of the performance and stability of two torsional vibration dampers for variable-speed wind turbines

John Licari, Carlos E. Ugalde-Loo, Janaka B. Ekanayake and Nick Jenkins

Institute of Energy, Cardiff School of Engineering, Cardiff University, CF24 3AA, Wales, UK

ABSTRACT

Alleviation of excess fatigue loads due to vibrations in the drive-train of wind turbines can be achieved through the use of torsional vibration dampers. Two torsional dampers based on different design approaches were designed and assessed: the first employs a conventional band-pass filter technique, whereas the second involves an alternative model-based approach. Frequency domain analyses were carried out on the system with the two dampers for the cases with and without model uncertainty. The system using the band-pass filter-based damper showed deterioration in stability and performance when subjected to uncertainty in the model and had to be re-tuned to recover a good damping performance. Conversely, the system employing the model-based damper maintained good stability and superior damping performance in the presence of model uncertainties. These attributes can ensure that the damper exhibits a good performance even if the wind turbine parameters vary during operation, such as when ice forms on the blades. Time domain simulations were carried out to verify the frequency domain analyses. © 2014 The Authors. *Wind Energy* published by John Wiley & Sons, Ltd.

1. INTRODUCTION

The evolution of wind energy technology over the last decades has led to increased rotor diameters and the overall size of wind turbines (WTs). Achieving a better cost effectiveness is now an important challenge faced by manufacturers. To this end, a reduction of component masses has been the preferred approach, although this results in turbines less tolerant to fatigue loads.[1] The value of wind energy generation is largely determined by four factors: installed capital cost, annual operating expenses, value of annual energy production and the cost of financing a WT.[2,3] By minimising the capital cost and annual operating expenses such as maintenance costs, generation value may be increased.[4]

This study focuses on the mitigation of torsional vibrations in a variable-speed WT drive-train. A drive-train sub-assembly is composed of the rotor hub, low-speed shaft (LSS), bearings, gearbox, high-speed shaft (HSS), couplings and the generator. Mechanical transient loads (e.g. wind gusts) can excite modes, which in turn may reflect on large torsional vibrations in the drive-train. These modes include the drive-train mode itself and the blade in-plane symmetrical modes.[5] Significant stress will result if these vibrations are left unaddressed; as a consequence, this can lead to lifetime reduction of components such as the gearbox.[6,7]

Damping of torsional vibrations can be accomplished using passive and active systems. Passive systems include additional mechanical components. Damping is achieved through appropriately designed rubber mounts or couplings.[8] In active systems, mitigation is carried out by making use of the generator torque and pitch control.[9–13] In the pitch control approach, the blades are utilised to produce a torque component that opposes the change in rotor speed. However, this

reduces slightly the energy output as the turbine is no longer operating at optimum pitch. Additionally, the pitch system becomes more active, demanding faster pitching rates.[10,11]

The most effective approach for the mitigation of torsional vibrations is obtained by using the generator torque.[14] This provides an auxiliary damping torque component to include additional damping to the system. The conventional design approach for torsional vibration dampers employs fixed parameter band-pass filters (BPFs).[5,15–17] Previous work has shown that the drawback of this damper is that its damping performance and the stability of the system can be compromised if the vibration frequencies are not identified exactly.[18] This can occur in the presence of model uncertainty (e.g. differences between the actual WT and the model adopted for control system design) or parameter variations during operation.[19–21] Therefore, model uncertainties and parameter variations will effectively shift the vibration frequencies of the system, and thus, the fixed parameter BPF-based damper has to be re-tuned to cater for such variations.[18] To ensure good damping performance and stability of the system without any re-tuning, a model-based damper is proposed.

In this study, two torsional dampers were designed, formally analysed and implemented: one is based on the conventional design approach (BPFs), and the other is based on a model-based approach. A frequency domain analysis was conducted to assess and compare the stability of the system and the performance of the dampers when subjected to WT model uncertainties. This analysis was verified by performing simulations on a WT model developed in MATLAB/Simulink® (The MathWorks, Inc, Natick, Massachusetts, United States). Simulations for a wind step and turbulent wind events were carried out for the cases with and without model uncertainties. All simulations were performed for above rated wind speed operation—torsional vibrations are most significant in this region, where the generator torque is maintained at its rated value and the pitch controller is in service.[17]

The main contributions of this paper are a demonstration through analysis and validation through simulations that model-based torsional dampers are capable of maintaining a good damping performance upon the presence of model uncertainty. The model-based damper used in this work was proposed and implemented in Licari *et al.*[18] However, this paper builds on previous research by performing comprehensive performance and stability assessments—presented in a clear way that would be useful for a torsional damper designer. A thorough analysis of sensitivity and complementary sensitivity functions is carried out, showing that the proposed model-based approach exhibits adequate disturbance rejection and reference tracking properties as opposed to conventional damping schemes based on BPFs.

2. WT SYSTEM MODELLING

The block diagram of a permanent magnet synchronous generator (PMSG)-based variable-speed WT is shown in Figure 1. It consists of an aerodynamic model, a mechanical model of the drive-train including a three-stage gearbox, a generator model, a back-to-back voltage source converter (VSC), a pitch controller and a torsional vibration damper.

The control strategy was implemented through a torque controller to optimise power production (below rated wind speeds) and a pitch controller to limit aerodynamic power (above rated wind speeds). Since the focus of this study is the damping of torsional vibrations, the WT model was reduced to just the torque loop, as illustrated in Figure 2.

2.1. Electrical model

The PMSG was modelled in the rotor reference frame as given by equations (1)–(4), in which the *d*-axis is aligned with the rotor field and the *q*-axis leads the *d*-axis by 90°[12,22]:

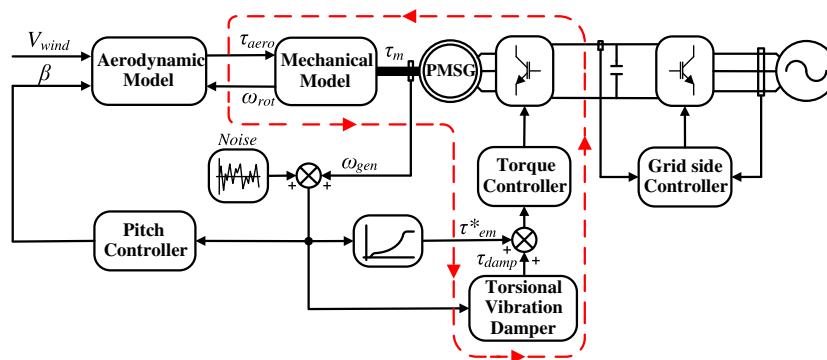$$v_d = R_s i_d + \frac{d}{dt}\lambda_d - \omega_e \lambda_q \tag{1}$$

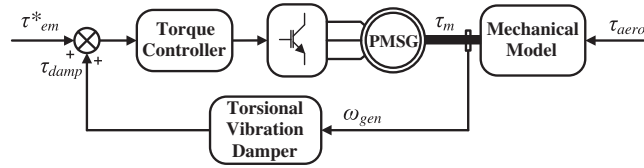

Figure 1. WT block diagram.[18]

Figure 2. Reduced block diagram of the torque loop.

$$v_q = R_s i_q + \frac{d}{dt}\lambda_q + \omega_e\lambda_d \tag{2}$$

$$\tau_e = {}^3/_2\, n_{pp}\left[\lambda_m i_q + \left(L_d - L_q\right)i_d i_q\right] \tag{3}$$

$$\begin{aligned}\lambda_d &= L_d i_d + \lambda_m \\ \lambda_q &= L_q i_q\end{aligned} \tag{4}$$

where L_d and L_q are the self-inductances, R_s is the stator winding resistance, i_d, v_d and i_q, v_q are the currents and voltages, λ_m is the flux induced by the permanent magnets, n_{pp} is the pole pairs number and ω_e is the electrical speed of the generator. Typically, a PMSG has low saliency, hence the *dq*-axis self-inductances can be assumed to be equal ($L_d \approx L_q$).[22] Under this condition, the electromagnetic torque will be proportional to the *q*-axis current only.

Typical control strategies for PMSGs are based on a two-step procedure. The first one consists of controlling the stator currents (the electrical dynamics) to decouple the *d*-axis and *q*-axis components. For instance, vector control schemes employ decoupling networks aiming to cancel the back electromotive force (EMF) terms.[22] The *q*-axis current open loop consists of the VSC, the controller (for instance a Proportional-Integral (PI) controller, but other control structures may be used) and the PMSG. Assuming that an adequate decoupling controller is in place, the closed-loop *dq* currents will be independent of each other—and the electromagnetic torque will be dependent on the *q*-axis current loop dynamics only. The slowest pole of the *q*-axis current open loop is associated with the PMSG and is governed by the electrical time constant (L_q / R_s). This is much smaller than the mechanical time constant of the system, governed by the generator and turbine inertias. Because of this bandwidth separation, the electrical dynamics can be assumed to be in steady state when addressing the mechanical dynamics. This is a common practice when carrying out the second step of the procedure, which is the design of the PMSG speed controller.[13,23] Therefore, the PMSG electrical subsystem, the VSC and the torque controller were modelled as a first-order lag with a time constant *T* as shown in Figure 3. All parameters are provided in Appendix A.

2.2. Mechanical model

The mechanical model consists of the rotor, the gearbox and the generator. In the study of torsional vibrations, it is important to consider the coupling of the blade in-plane symmetrical mode to the drive-train.[16,17] This is because if the blade in-plane mode is excited, it can lead to torsional vibration because of the coupling with the drive-train.

In reality, the representation of the blade bending dynamics is dependent on the non-uniform distribution of the mass, stiffness and twist angle of the blade. Finite element techniques can be used to represent the dynamic characteristics of the rotating blades, but this approach is not easily integrated into simulation software such as MATLAB/Simulink. An alternative option is to obtain a model that simplifies the rotor dynamics as much as possible while still capturing the natural frequency of the blade (relevant to torsional vibrations). To achieve this, the blades in-plane bending dynamics were represented as the torsional system shown in Figure 4(a).[24–26] Since the blade bending occurs at a considerable distance from the joint between the blade and the hub, the blades were divided into two sections: a rigid and a flexible part. The rigid part is formed by the inertia of the rigid part of the blade and the hub inertia. This is in turn connected to the flexible part of
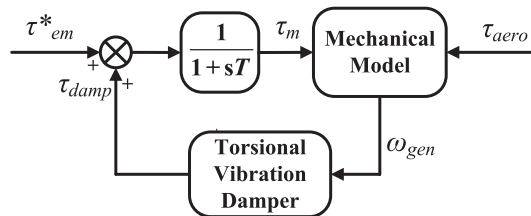

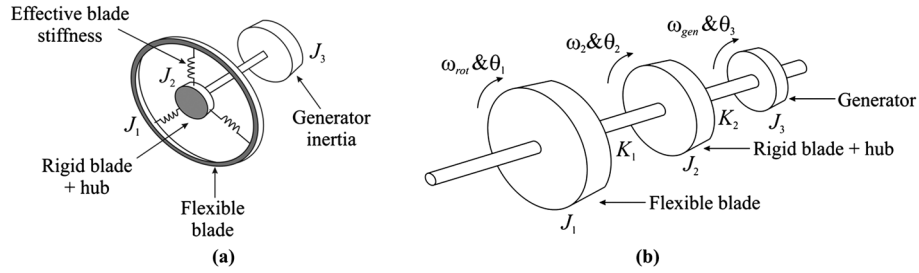**Figure 3.** Simplified model used for the frequency domain analysis.

Figure 4. Mechanical model: (a) equivalent torsional representation; (b) three-mass representation.[24]

the blade through three springs, which represent the flexibility of the individual blades. The simplified rotor structure (Figure 4(a)) was modelled as a three-mass model considering both the drive-train and blade in-plane modes, shown in Figure 4(b). This mechanical system was first presented in the work by Ramtharan *et al.*[24] for the study of rotor structural modelling effects on the electrical transient performance of a WT.

The three-mass mechanical system referred to the LSS was modelled as[24]

$$J_1 \frac{d}{dt}\omega_{rot} = \tau_{aero} - K_1(\theta_1 - \theta_2) \tag{5}$$

$$J_2 \frac{d}{dt}\omega_2 = -K_1(\theta_2 - \theta_1) - K_2\left(\theta_2 - \frac{\theta_3}{N_{gear}}\right) \tag{6}$$

$$J_3 \frac{d}{dt}\omega_{gen} = -\tau_m - K_2\left(\frac{\theta_3}{N_{gear}} - \theta_2\right) \tag{7}$$

$$\frac{d}{dt}(\theta_1 - \theta_2) = (\omega_{rot} - \omega_2) \tag{8}$$

$$\frac{d}{dt}(\theta_2 - \theta_3) = (\omega_2 - \omega_{gen}) \tag{9}$$

where J_1 represents the inertia of the effective flexible part of the blades, J_2 the inertia of the hub and the rigid part of the blades, J_3 the inertia of the generator, K_1 the effective blades stiffness, K_2 the resultant stiffness of the LSS and HSS, ω_{rot} the rotor speed, ω_{gen} the PMSG speed and N_{gear} the gearbox ratio. All system parameters referred to the LSS are listed in Appendix A. These were obtained by conducting a spectral analysis of the LSS torque in DNV GL Bladed (Høvik, Norway). Further information on this procedure is provided in the work by Licari *et al.*[27]

The inputs to the three-mass system are the mechanical opposing torque from the generator τ_m and the aerodynamic torque τ_{aero}, with τ_{aero} being considered as a disturbance. The output of the model is the generator speed ω_{gen}. The complete mechanical representation was expressed in state-space form as

$$\begin{aligned} \dot{\mathbf{x}} &= \mathbf{A}\mathbf{x} + \mathbf{B}u + \mathbf{B_d}u_d \\ y &= \mathbf{C}\mathbf{x} + \mathbf{D}u \end{aligned} \tag{10}$$

where $\mathbf{x} = [\omega_{rot}, (\theta_1 - \theta_2), \omega_2, (\theta_2 - \theta_3), \omega_{gen}]^T$, $u = \tau_m$, $u_d = \tau_{aero}$ and $y = \omega_{gen}$. Matrices are given in Appendix B.

2.3. Torsional vibration dampers

The two different schemes employed in this paper are presented next.

2.3.1. BPF-based damper.
The block diagram for this damper is illustrated in Figure 5. The damper structure adopted in this work employs a notch filter in series with two BPFs.

Common practice suggests the use of a second-order BPF, which extracts the vibration frequency from the speed of the PMSG.[15,16] This signal, which effectively adds a small ripple to the torque demand of the generator (τ_{em}^*) at the vibration frequencies, is employed to mitigate torsional vibrations. However, since the nominal mechanical frequencies associated to the model described by equations (5)–(9) are sufficiently apart (i.e. 2.54 and 3.7 Hz[27]), two suitably tuned BPFs have been included to address each one separately. If one BPF was used to cater for both, it would have required a high bandwidth, which is undesirable.[17] Each BPF has a transfer function of the form
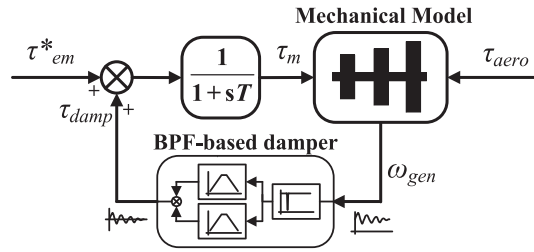
Figure 5. Torsional vibration damper based on BPF.[18]

$$G_{BPF}(s) = K \frac{2\zeta\omega_n s}{s^2 + 2\zeta\omega_n s + \omega_n^2} \tag{11}$$

where K is the DC gain, ω_n the undamped natural frequency and ζ the damping ratio.

The BPFs must limit the response outside their bandwidth to avoid the introduction of unwanted frequencies in the system (e.g. multiples of the blade passing frequencies, 3P and 6P). This can be achieved through a BPF design ensuring a low damping ratio (reflected as a narrow peak). However, since the 6P frequency (1.8 Hz) of the WT used was relatively close to the frequency of the blade in-plane mode (2.54 Hz), it was necessary to include a notch filter to limit the damper response at 1.8 Hz, as shown in Figure 5.[15] The transfer function of such a filter is given by

$$G_{NF}(s) = \frac{s^2 + 2\zeta_1\omega_{nf} s + \omega_{nf}^2}{s^2 + 2\zeta_2\omega_{nf} s + \omega_{nf}^2} \tag{12}$$

where ζ_1 and ζ_2 are the damping ratios setting the notch filter depth and ω_{nf} the notch frequency. All parameters (notch filter and BPFs) are given in Appendix C.

2.3.2. Model-based damper.

An alternative approach to mitigate torsional vibrations is shown in Figure 6. Here, the damping effect is achieved through a careful selection of the location of the blade in-plane and drive-train resonant closed-loop poles. In this case, this was carried out by employing a state feedback-based pole placement technique. Estimation of all state variables was carried out using an observer.

A Kalman filter (KF), a linear filter that minimises the variance of the estimation error, was included to achieve good state estimation in spite of process and measurement noise.[28,29] Except for the aerodynamic torque, the remaining inputs were available to the damper (i.e. the resultant generator torque reference and the generator speed). In the literature, two preferred methods are used to estimate the unknown aerodynamic torque input. The first one includes it in the general state estimation problem,[30–32] where the main difficulty is to determine which spectrum of wind to use.[33] Such a difficulty arises since WTs encounter different wind spectra depending on their locations. Additionally, the unsteady aerodynamic effects due to rotational sampling should be considered. This unsteadiness is due to the difference in wind speeds experienced by the rotor as it rotates, which in turn produces cyclic perturbations on the thrust forces and the rotational torque.[34] The second method estimates τ_{aero} by solving equation (5)—using the rotor speed derivative. Although this procedure is sensitive to measurement noise,[33] it was followed in this work to avoid the high sensitiveness to the accuracy of the wind spectrum. To suppress the noise resulting from derivatives, the generator speed was filtered through a low-pass filter prior
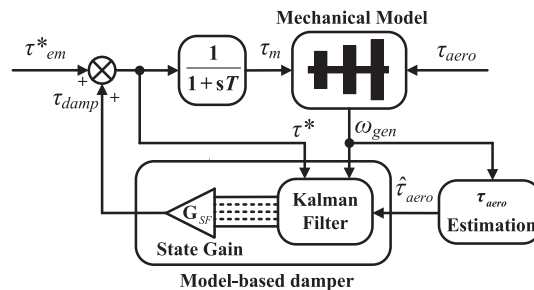

Figure 6. Model-based torsional vibration damper block diagram.[18]

to differentiating it. This introduced a time delay in the estimation of the aerodynamic torque. Long delays would hinder the operation of the KF and therefore affect the damper performance.[35] In order to prevent this, a compromise was reached between estimation delay and measurement noise rejection.

The model-based damper design was split into two separate stages. In the first stage, all states were assumed available for state feedback in order to obtain the state feedback gain $\mathbf{G}_{SF}$. As a second step, the state variables were estimated through a KF. When designing the KF, it was assumed that (i) the control model used was sufficiently accurate, (ii) disturbances (process and measurement noise) were stochastic and zero mean and (iii) process noise and measurement noise covariance matrices $\mathbf{Q}$ and $\mathbf{R}$ were known.[28] $\mathbf{R}$ was first computed through off-line sample measurements, followed by calculation of $\mathbf{Q}$ through a systematic trial and error approach—since $\mathbf{Q}$ is generally more difficult to obtain.[29]

Controllers based on state feedback and KFs, when employed individually, feature strong robustness characteristics. Unfortunately, if a KF provides the state estimation for a state feedback controller the system robustness drastically reduces. To overcome this issue, loop transfer recovery is normally utilised to retrieve some robustness.[36] In this work, the adjustment procedure proposed in the work by Doyle and Stein[37] was used. The ideal full state-feedback loop is achieved by modifying the design of the KF, where the uncertainties are represented by a large amount of process noise. Further details on the KF mathematical representation are given in the work by Simon and Welch and Bishop.[28,29] Parameters for the model-based damper are provided in Appendix C.

3. STABILITY AND PERFORMANCE ANALYSES

Stability and performance analyses were carried out on the system for the two torsional vibration dampers, and results are presented in Sections 3.1 and 3.2. The system was subjected to model uncertainty, which affected the nominal vibration frequencies F_{1nom} and F_{2nom} (2.54 and 3.7 Hz, respectively[27]). The uncertainty was introduced through variations of stiffness and inertia (J_i and K_i) in the three-mass model. A ±10% uncertainty bound on F_{1nom} (i.e. ±0.25 Hz) was assumed. A set of plant models was generated within the uncertainty bound at an interval of ±0.125 Hz. The set was divided in two groups to facilitate the identification of the uncertainty zones for which the stability and performance of the system can be compromised. The Bode plot of Figure 7(a) illustrates the set of plant models as the uncertainty in F_1 (ΔF_1) is below the nominal frequency (F_{1nom}) for all possible uncertainty in F_2 (ΔF_2), whereas Figure 7(b) shows the cases where ΔF_1 is above F_{1nom} for all possible ΔF_2.

3.1. Stability analysis

A feedback control system possesses robust stability if it remains stable when subjected to a specified range of process perturbations.[38] It has been reported that adequate stability margins are in the range of 10 dB and 60° [gain margin (GM) and phase margin (PM)].[39]

A stability analysis was performed to identify operating regions where the system has susceptibility to become unstable when subjected to vibration frequency uncertainty. This was carried out using the Nyquist stability criterion, with the classical GM and PM being employed to assess stability. The plant representing the torque loop in Figure 3 is open loop stable. For these kinds of plants, the criterion states that stability in the closed-loop is kept if no encirclements to the critical point $(-1, j0)$ exist.[40] The only drawback with these margins is that they do not provide information on how close the Nyquist
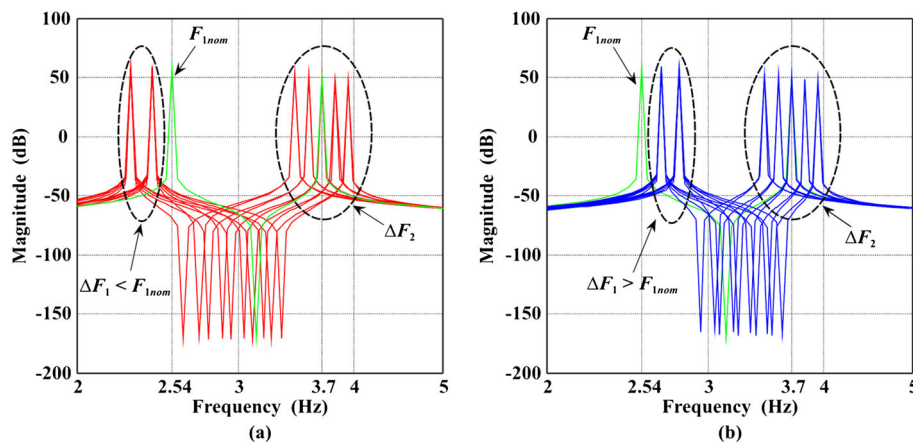

Figure 7. Set of plant models as (a) ΔF_1 is varied below F_{1nom} for all possible ΔF_2 and (b) ΔF_1 is varied above F_{1nom} for all possible ΔF_2.

path is to $(-1, j0)$. In order to obtain a measure of the distance from the critical point to any point on the Nyquist trajectory, the sensitivity function given by equation (13) was used[40]:

$$S = \frac{1}{1 + G(j\omega)C(j\omega)} = \frac{1}{1 + L(j\omega)} \tag{13}$$

where $G(j\omega)$, $C(j\omega)$ and $L(j\omega)$ are the plant, the damper and the open loop transfer functions, respectively. The term $1 + L(j\omega)$ in equation (13) can be represented as a vector from the critical point to any point on the Nyquist path, $L(j\omega)$, as shown in Figure 8.

The plant uncertainty $\Delta G(j\omega)$ is represented as a disc with radius $|\Delta G(j\omega)\,C(j\omega)|$ centred at each ω evaluated. As long as $|\Delta G(j\omega)\,C(j\omega)|$ is smaller than the distance $|1 + L(j\omega)|$, the Nyquist path will not encircle the critical point $(-1, j0)$ under the uncertainty bound $\Delta G(j\omega)$.

The complementary sensitivity function, T, which gives information on the amplification from the reference signal to the output signal given by equation (14), was used to determine the maximum uncertainty the system can experience without compromising stability.[40]

$$T = \frac{G(j\omega)C(j\omega)}{1 + G(j\omega)C(j\omega)} \tag{14}$$

Thus, the condition for the system to be robust stable is given by[41]

$$|C(j\omega)\Delta G(j\omega)| < |1 + L(j\omega)| \Rightarrow |\Delta G(j\omega)| < \left|\frac{1 + G(j\omega)C(j\omega)}{C(j\omega)}\right| \equiv \left|\frac{\Delta G(j\omega)}{G(j\omega)}\right| < \frac{1}{|T|} \; \forall \, \omega \geq 0 \tag{15}$$

The Nyquist diagrams for the system including the torsional dampers presented in Section 2, for all plant sets, are shown in Figure 9. For clarity, only the positive frequencies are shown.

It can be noted from Figure 9(a) that the BPF-based damper with the nominal plant model has good stability margins (GM = 8 dB, PM = 34°). However, as uncertainty in the vibration frequency was introduced, specifically when F_1 was lower than F_{1nom}, the stability margins decreased. This indicates that as the uncertainty increases beyond the low vibration frequency, the system becomes more susceptible to instability. At maximum uncertainty on the lower vibration frequency (-0.25 Hz), the system approached the critical point $(-1, j0)$. This implies that if either the BPF gain or the uncertainty bound increases slightly, the system will become unstable since the Nyquist plot would encircle $(-1, j0)$. In spite of having a large reduction in the stability margins, the system still can be regarded as being robust stable for an uncertainty bound ± 0.25 Hz; however, performance is expected to deteriorate considerably.

Figure 9(b) shows the Nyquist diagrams for the system employing the model-based damper. With the nominal plant model, the system has better stability margins (GM $\approx \infty$ dB, PM = 76°) than the system employing a BPF-based damper. The corresponding change in stability margins was very small when the vibration frequency uncertainty was introduced; hence, the use of the model-based damper ensures a robust stable system. Moreover, in the worst case within the uncertainty bound, the system still exhibited good stability margins (GM $\approx \infty$ dB, PM = 65°). Therefore, it is expected that the performance of the system will not change much when subjected to model uncertainties.

Furthermore, the complementary sensitivity function T was plotted for the system equipped with the different dampers to determine the maximum uncertainty it can experience without compromising stability. This is shown in Figure 10.
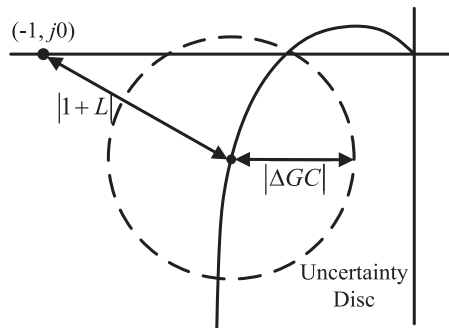

Figure 8. Nyquist plot of the nominal loop transfer function G(jω)C(jω) with plant uncertainty G(jω).[41]
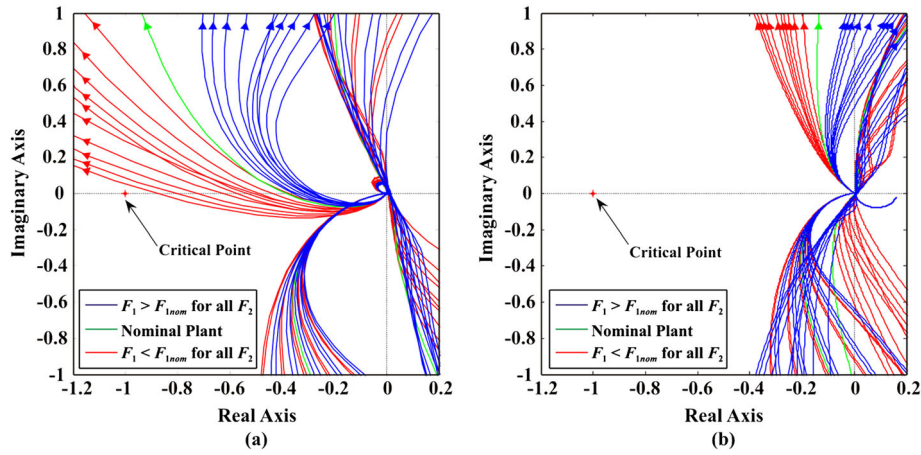
Figure 9. Nyquist plots with vibration frequency uncertainty for (a) BPF-based damper and (b) model-based damper.
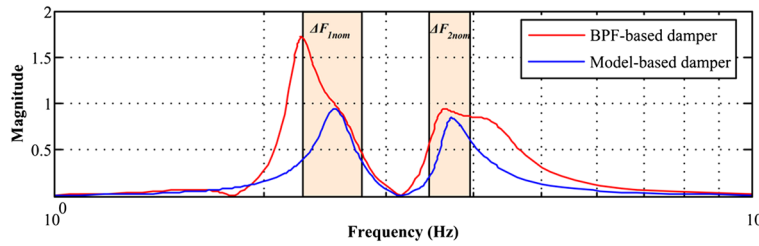

Figure 10. Complementary sensitivity function T.

Recalling from equation (15), the larger the magnitude of *T*, the smaller the allowable disturbance is. Within the region of the vibration frequencies uncertainty (ΔF_1 and ΔF_2 in Figure 10), the maximum uncertainty for the system using the model-based damper is (max| *T* |= 0.95). Conversely, for the system employing the BPF-based damper, (max| *T* |= 1.7). From equation (15), this implies that the maximum allowable uncertainty for the system using the model-based damper is $|\Delta G(j\omega)| = |1.05 \times G(j\omega)|$; this figure decreases to $|\Delta G(j\omega)| = |0.59 \times G(j\omega)|$ when the BPF-based damper is used.

The plots of Figure 10 indicate that if the model-based damper is used, a higher model uncertainty can be tolerated before the system becomes unstable. Therefore, it is more robust than the system with the BPF-based damper.

3.2. Performance analysis

In addition to ensuring stability, it is also important to investigate whether the system possesses robust performance in the presence of vibration frequency uncertainty. Robust performance can be defined as the low sensitivity of system performance with respect to model uncertainties and disturbances.[36] In this section, the system response to input disturbances, measurement noise and reference signal tracking was analysed. An equivalent block diagram of the system with unity feedback in presence of disturbance, *d* and measurement noise, *n* is shown in Figure 11.

3.2.1. Disturbance rejection.
The transfer function relating the output of the system (*y*) for a plant disturbance input (*d*) is given by

$$G_{YD}(j\omega) = \frac{Y(j\omega)}{D(j\omega)} = \frac{G(j\omega)}{1 + G(j\omega)C(j\omega)} = S \times G(j\omega) \tag{16}$$
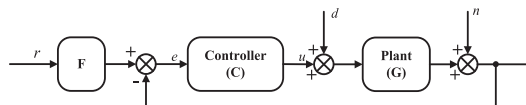

Figure 11. System block diagram with process disturbance, d and measurement noise, n.[24]

The magnitude of S (i.e. the sensitivity function defined by equation (13)) quantifies the amplification level provided by the system for input disturbance (d) for all ω. Thus, the smaller is S, the better is the disturbance rejection. Differentiating equation (16) yields[41]

$$\frac{dG_{YD}(j\omega)}{dG(j\omega)} = \left(\frac{1 + G(j\omega)C(j\omega) - G(j\omega)C(j\omega)}{(1 + G(j\omega)C(j\omega))^2}\right) = S \times \frac{G_{YD}(j\omega)}{G(j\omega)} \Rightarrow \frac{dG_{YD}(j\omega)}{G_{YD}(j\omega)} = S \times \frac{dG(j\omega)}{G(j\omega)} \tag{17}$$

which shows that the effect of small variations (model uncertainties) in $G(j\omega)$ on G_{YD} ($j\omega$) is also dependent on S. Typically, the plant disturbances are low frequency variations. Hence, $|S(j\omega)|$ needs to be small at low frequencies. A plot of S at low frequencies is shown in Figure 12. It can be observed that the system with the model-based damper has better disturbance rejection than the BPF-based damper.

It is also important for the system that the control actions for measurement noise are as small as possible. The transfer function relating the controller action (u) and the noise input (n) is given by

$$G_{UN}(j\omega) = \frac{U(j\omega)}{N(j\omega)} = \frac{C(j\omega)}{1 + G(j\omega)C(j\omega)} = \frac{T}{G(j\omega)} \tag{18}$$

Measurement noise is typically high frequency noise; thus, T has to be small at high frequencies to have low control actions.[41] A plot of T at high frequencies is shown in Figure 13.

It can be observed that both systems have good measurement noise rejection; however, the system with the model-based damper exhibits a better rejection.

The variation of G_{UN} ($j\omega$) with small variations in $G(j\omega)$ is also dependent on T, as given by

$$\frac{dG_{UN}(j\omega)}{dG(j\omega)} = \left(\frac{-C(j\omega)^2}{(1 + G(j\omega)C(j\omega))^2}\right) = T \times \frac{G_{UN}(j\omega)}{G(j\omega)} \Rightarrow \frac{dG_{UN}(j\omega)}{G_{UN}(j\omega)} = T\frac{dG(j\omega)}{G(j\omega)} \tag{19}$$

Hence, the effects of plant variations on G_{UN} ($j\omega$) are minimal since T is small at high frequencies, as shown in Figure 13.
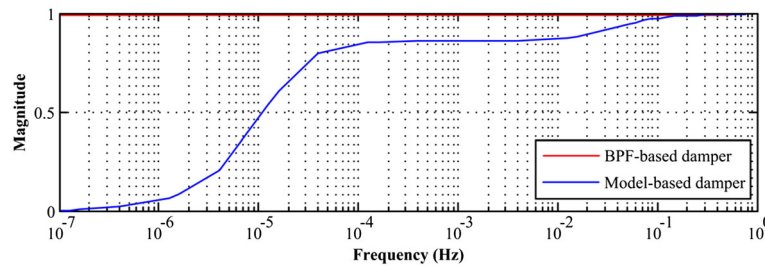

Figure 12. Sensitivity function at low frequencies.
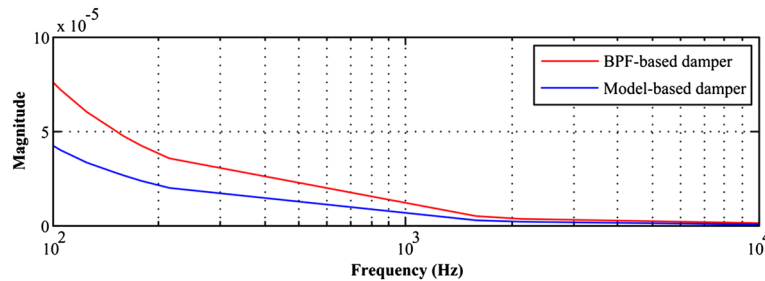

Figure 13. Complementary sensitivity function at high frequency.

3.2.2. Reference signal tracking.

The closed-loop transfer function of the system is given by

$$G_{YR}(j\omega) = \frac{Y(j\omega)}{R(j\omega)} = \frac{F(j\omega)G(j\omega)C(j\omega)}{1 + G(j\omega)C(j\omega)} \tag{20}$$

The variation of the $G_{YR}(j\omega)$ with small variations in $G(j\omega)$ is dependent on S as given by

$$\frac{dG_{YR}(j\omega)}{dG(j\omega)} = \frac{C(j\omega)F(j\omega)}{(1 + G(j\omega)C(j\omega))^2} = S\frac{G_{YR}(j\omega)}{G(j\omega)} \implies \frac{dG_{YR}(j\omega)}{G_{YR}(j\omega)} = S\frac{dG(j\omega)}{G(j\omega)} \tag{21}$$

In order to have good tracking of the reference signal, it is important that S is unity everywhere except at the areas of potential resonances. A plot of the sensitivity function is shown in Figure 14. It can be observed that the sensitivity function of the system with a BPF-based damper has a very high peak close to the area of uncertainty ΔF_1. This means that the system will amplify any frequencies where S is greater than unity. The sensitivity function for the system using the model-based damper is less than unity in most of the vibration frequency uncertainty areas. This indicates that any frequency within the area of uncertainty will be damped.

The closed-loop Bode diagrams for the two plant sets were also plotted to observe how the system response is affected with vibration frequency uncertainty. These are shown in Figure 15. It is evident from Figure 15(a) that there is a resonant peak for the system using the BPF-based damper. This is a consequence of the sensitivity function being larger than unity close to the frequency uncertainty area and implies that the BPF-based damper performance is being compromised. The closed-loop plots for the system employing the model-based damper are shown in Figure 15(b). It can be noted that there are no resonant frequency peaks in this case, which gives an indication of good damping performance.
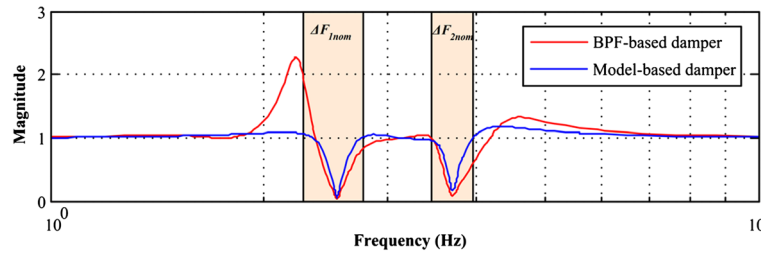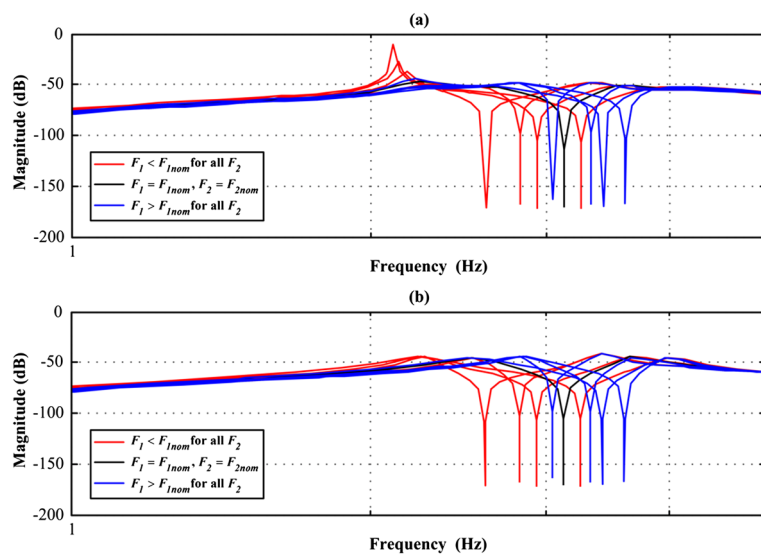

Figure 14. Sensitivity function.

Figure 15. Closed-loop Bode plots (a) system with the BPF-based damper and (b) system with model-based damper.

4. TIME DOMAIN SIMULATIONS

Time domain simulations were carried out to verify the performance of both torsional vibration dampers when subjected to vibration frequency uncertainty ($F_1 = F_{1nom} - 0.25\,\text{Hz} = 2.29\,\text{Hz}$, $F_2 = F_{2nom} + 0.25\,\text{Hz} = 3.95\,\text{Hz}$). In order to achieve this,
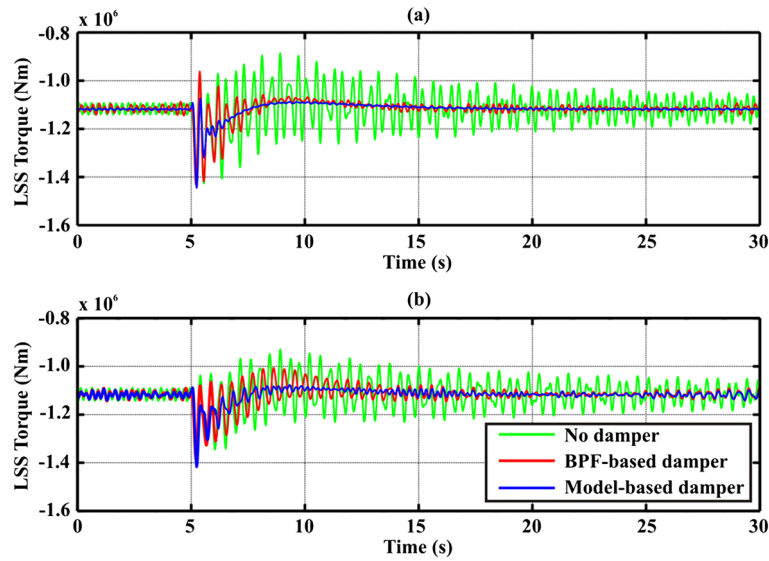
Figure 16. LSS torque for a wind step (a) plant with nominal vibration frequencies and (b) plant with vibration frequencies uncertainty.
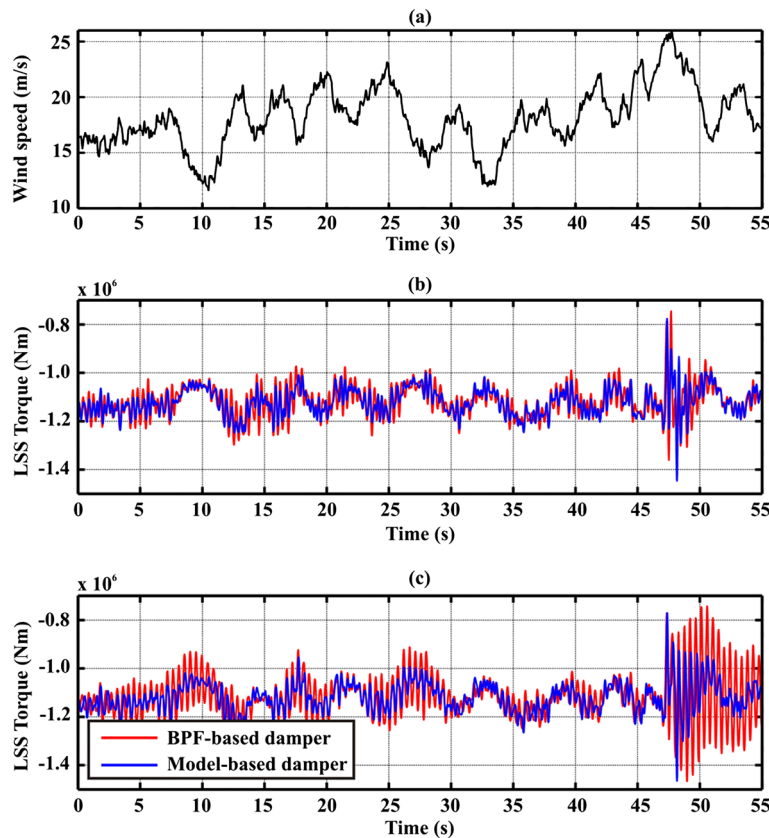
Figure 17. LSS torque for a turbulent wind (a) wind profile, (b) plant with nominal vibration frequencies, and (c) plant with vibration frequencies uncertainty.

the system illustrated in Figure 1 was implemented in Simulink and was tested for two cases: a wind step and a turbulent wind. In the first case, a step in wind speed from 16 to 22 m s^{-1} at 5 s was applied to excite the mode frequencies of the system. In the second case, a turbulent wind with a mean of 18 m s^{-1} and turbulence intensity of 12% based on Kaimal spectra was used. Measurement noise was included to make the simulation more realistic. This was achieved by adding white Gaussian noise (zero mean, 0.5 rad s^{-1} standard deviation) to the PMSG speed. The torque in the LSS was selected as the basis for comparison of the torsional vibration dampers performance. Figures 16 and 17 show the results of the LSS torque for the wind step and wind turbulent cases, respectively.

From the figures, it can be observed that although both systems were stable, the system employing the model-based damper featured a superior performance in damping torsional vibrations, particularly when model uncertainty was considered. In fact, the BPF-based damper performance was compromised when model uncertainty was present, and re-tuning of the damper was necessary in order to recover its damping performance.

5. CONCLUSION

Two torsional vibration dampers were designed and assessed. Stability and performance analyses have been conducted on the system with the two dampers. This was carried out to evaluate the robustness of the system when model uncertainties are present. The stability analysis showed that without model uncertainty, the system exhibited good stability margins for both damper designs. Nevertheless, when model uncertainty was introduced, the stability margins using the BPF-based damper decreased dramatically, whereas they hardly changed when the model-based damper was employed. This was also confirmed through assessment of the complementary sensitivity function.

An analysis was carried out to evaluate the effect of model uncertainty on the system performance. The system using the model-based damper showed better rejection of both process disturbance and measurement noise as opposed to the system equipped with a BPF-based damper. Moreover, when the model-based damper was used, the system showed good attenuation within the uncertainty area; on the other hand, amplification was present with a BPF-based damper. This effect was clearly observed in the closed-loop response plots.

Simulation results demonstrated that the system equipped with the model-based damper exhibited a superior damping performance compared with its BPF-based damper counterpart—particularly under the inclusion of model uncertainty. In order to recover its damping performance exhibited when uncertainty was not present, the BPF-based damper needed to be re-tuned. Conversely, the performance achieved with the model-based design was not affected when model uncertainty was introduced. Therefore, the model-based damper can be used to ensure damping of torsional vibrations when parameters vary during operation of the WT (e.g. ice on the blades). Moreover, this attribute can be used to eliminate re-tuning operations during commissioning of WTs—carried out for BPF-based designs to ensure an adequate damping performance. The only downside is that the use of a model-based damper implies a more challenging design process compared with its BPF-based counterpart.

ACKNOWLEDGEMENT

APPENDIX A

2 MW WT parameters:

Rated speed = 18 rpm, rotor diameter = 38.75 m, blades = 3, $J_1 = 3.9196 \times 10^6$ kg·m^2, $J_2 = 2.1094 \times 10^6$ kg·m^2, $K_1 = 4.5979 \times 10^8$ N·m rad^{-1}, $K_2 = 1.6 \times 10^8$ N·m rad^{-1}, $N_{gear} = 83.33 : 1$.

PMSG parameters:

Power rating = 2 MW, $J_3 = 416633$ kg m^2, poles = 4, rated frequency = 50 Hz, $R_s = 4.523$ mΩ, $L_d = L_q = 322$ μH, $T = L_q/R_s$.

Pitch controller parameters:

Proportional gain $K_p = 9.86 \times 10^{-3}$, integral gain $K_i = 3.4 \times 10^{-3}$, actuator model time constant $= 0.3$ s, pitch angle limits $=$ min $-2°$, max $90°$, pitch rate limit $= \pm 8° \, \text{s}^{-1}$.

APPENDIX B

Mechanical model:

$$\mathbf{A} = \begin{bmatrix} 0 & -\dfrac{K_1}{J_1} & 0 & 0 & 0 \\ 1 & 0 & -1 & 0 & 0 \\ 0 & \dfrac{K_1}{J_2} & 0 & -\dfrac{K_2}{J_2} & 0 \\ 0 & 0 & 1 & 0 & -\dfrac{1}{N_{gear}} \\ 0 & 0 & 0 & \dfrac{N_{gear}K_2}{J_3} & 0 \end{bmatrix}, \mathbf{B} = \begin{bmatrix} 0 & 0 & 0 & 0 & \dfrac{N_{gear}{}^2}{J_3} \end{bmatrix}^T,$$

$$\mathbf{B}_d = \begin{bmatrix} -\dfrac{1}{J_1} & 0 & 0 & 0 & 0 \end{bmatrix}^T, \mathbf{C} = \begin{bmatrix} 0 & 0 & 0 & 0 & 1 \end{bmatrix}, \mathbf{D} = 0$$

APPENDIX C

BPF-based damper:

BPF1: $K = 400$, $\xi = 0.15$, $F_c = 2.4$ Hz, BPF2: $K = 400$, $\xi = 0.15$, $F_c = 3.9$ Hz. Notch filter: $\xi_1 = 0.0015$, $\xi_2 = 0.14$, $F_c = 1.8$ Hz.

Model-based damper:

$$\mathbf{G}_{SF} = [G_1, \ G_2, \ G_3, \ G_4, \ G_5] = [6.36 \times 10^4, -4.29 \times 10^5, -1.36 \times 10^3, 1.81 \times 10^5, -5.99 \times 10^2],$$

$$\mathbf{R} = 0.25,$$

$$\mathbf{Q}_f = \begin{bmatrix} 2.56 \times 10^{-11} & 0 & 0 & 0 & 0 \\ 0 & 3 \times 10^{-15} & 0 & 0 & 0 \\ 0 & 0 & 6.22 \times 10^{-12} & 0 & 0 \\ 0 & 0 & 0 & 2.42 \times 10^{-11} & 0 \\ 0 & 0 & 0 & 0 & 1.649 \times 10^{-3} \end{bmatrix}$$

REFERENCES

1. Østergaard KZ, Brath P, Stoustrup J. Gain-scheduled linear quadratic control of wind turbines operating at high wind speed. In *IEEE International Conference on Control Applications (CCA)*, Singapore, 1-3 October, 2007; 276–281. DOI: 10.1109/cca.2007.4389243.
2. Tegen S, Lantz E, Hand M, Maples B, Smith A, Schwabe P. 2011 cost of wind energy review. 2013. [Online]. Available: www.nrel.gov/docs/fy13osti/56266.pdf. (Accessed 30th March 2014)
3. US Department of Energy. 20% Wind energy by 2030 report. 2008. [Online]. Available: www.osti.gov/bridge. (Accessed 30th March 2014)

4. Kusiak A, Zhang Z. Control of wind turbine power and vibration with a data-driven approach. *Renewable Energy* 2012; **43**: 73–82. DOI: 10.1016/j.renene.2011.11.024.

5. Bossanyi EA. Controller for 5MW reference turbine. 2009. [Online]. Available: www.upwind.eu/. (Accessed 30th March 2014)

6. Molinas M, Suul JA, Undeland T. Extending the life of gear box in wind generators by smoothing transient torque with STATCOM. *IEEE Transactions on Industrial Electronics* 2010; **57**: 476–484. DOI: 10.1109/tie.2009.2035464.

7. Caselitz P, Kleinkauf W, Krüger T, Petschenka J, Reichardt M, Störzel K. Reduction of fatigue loads on wind energy converters by advanced control methods. In *European Wind Energy Conference (EWEC)*. Dublin, Ireland, 1997; 555–558.

8. Westlake AJG, Bumby JR, Spooner E. Damping the power-angle oscillations of a permanent-magnet synchronous generator with particular reference to wind turbine applications. *IEE Proceedings - Electric Power Applications* 1996; **143**: 269–280. DOI: 10.1049/ip-epa:19960285.

9. Wasynczuk O, Man DT, Sullivan JP. Dynamic behavior of a class of wind turbine generators during random wind fluctuations. *IEEE Power Engineering Review* 1981; **1**: 47–48. DOI: 10.1109/mper.1981.5511593.

10. Jockel S, Hartkopf T, Hagenkort B, Schneider H, Ruckh A. Direct-drive synchronous generator system for offshore wind farms with active drive train damping by blade pitching. In *European Wind Energy Conference (EWEC)*. Copenhagen, Denmark, 2001; 991–994.

11. Wright AD. *Modern Control Design for Flexible Wind Turbines*. NREL: Colorado, 2004; 233.

12. Hansen AD, Michalke G. Modelling and control of variable-speed multi-pole permanent magnet synchronous generator wind turbine. *Wind Energy* 2008; **11**: 537–554. DOI: 10.1002/we.278.

13. Geng H, Xu D, Wu B, Yang G. Comparison of oscillation damping capability in three power control strategies for PMSG-based WECS. *Wind Energy* 2011; **14**: 399–406. DOI: 10.1002/we.428.

14. Wright AD, Fingersh LJ. Part I: control design, implementation, and initial tests. *Advanced Control Design for Wind Turbines*. NREL: Colorado, 2008.

15. Bossanyi EA. The design of closed loop controllers for wind turbines. *Wind Energy* 2000; **3**: 149–163. DOI: 10.1002/we.34.

16. Bossanyi EA. Wind turbine control for load reduction. *Wind Energy* 2003; **6**: 229–244. DOI: 10.1002/we.95.

17. Burton T, Sharpe D, Jenkins N, Bossanyi E. *Wind Energy Handbook*. John Wiley & Sons Ltd: Chichester, 2002; 642.

18. Licari J, Ugalde-Loo CE, Ekanayake JB, Jenkins N. Damping of torsional vibrations in a variable-speed wind turbine. *IEEE Transactions on Energy Conversion* 2013; **28**: 172–180. DOI: 10.1109/tec.2012.2224868.

19. Licari J, Ugalde-Loo CE, Ekanayake J, Jenkins N. Comparison of the performance of two torsional vibration dampers considering model uncertainties and parameter variation. In *European Wind Energy Association (EWEA) Annual Event*, 2012; 1–8.

20. Xing Z-X, Liang L-Z, Guo H-Y, Wang X-D. Damping control study of the drive train of DFIG wind turbine. In *International Conference on Energy and Environment Technology (ICEET)*, 16-18 Oct. 2009, 2009; 576–579. DOI: 10.1109/iceet.2009.146.

21. Dixit A, Suryanarayanan S. Towards pitch-scheduled drive train damping in variable-speed, horizontal-axis large wind turbines. In *44th IEEE Conference on Decision and Control and European Control Conference (CDC-ECC)*, Seville, Spain, 12-15 Dec., 2005; 1295–1300. DOI: 10.1109/cdc.2005.1582337.

22. Krishnan R. *Permanent Magnet Synchronous and Brushless DC Motor Drives*. Taylor & Francis: Boca Raton, 2010.

23. Geng H, Xu D, Wu B, Yang G. Active damping for PMSG-based WECS with DC-link current estimation. *IEEE Transactions on Industrial Electronics* 2011; **58**: 1110–1119. DOI: 10.1109/tie.2010.2040568.

24. Ramtharan G, Jenkins N, Anaya-Lara O, Bossanyi E. Influence of rotor structural dynamics representations on the electrical transient performance of FSIG and DFIG wind turbines. *Wind Energy* 2007; **10**: 293–301. DOI: 10.1002/we.221.

25. Li H, Chen Z. Transient stability analysis of wind turbines with induction generators considering blades and shaft flexibility. In *33rd Annual Conference of the IEEE Industrial Electronics Society (IECON)*, Taipei, 5-8 Nov., 2007; 1604–1609. DOI: 10.1109/iecon.2007.4460348.

26. Ramtharan G. *Control of Variable Speed Wind Generators*. PhD dissertation. The University of Manchester: Manchester, 2008.

27. Licari J, Ugalde-Loo CE, Liang J, Ekanayake J, Jenkins N. Torsional damping considering both shaft and blade flexibilities. *Wind Engineering* 2012; **36**: 181–196. DOI: 10.1260/0309-524x.36.2.181.

28. Simon D. *Optimal State Estimation*. John Wiley & Sons: Canada, 2006.
29. Welch G, Bishop G. An introduction to the Kalman filter. SIGGRAPH; 2001. [Online]. Available: www.cs.unc.edu/~welch/media/pdf/kalman_intro.pdf. (Accessed 30th March 2014)
30. Billy Muhando E, Senjyu T, Urasaki N, Yona A, Kinjo H, Funabashi T. Gain scheduling control of variable speed WTG under widely varying turbulence loading. *Renewable Energy* 2007; **32**: 2407–2423. DOI: 10.1016/j.renene.2006.12.011.
31. Bourlis D, Bleijs JAM. A wind speed estimation method using adaptive Kalman filtering for a variable speed stall regulated wind turbine. In *IEEE 11th International Conference on Probabilistic Methods Applied to Power Systems (PMAPS)*, Singapore, 14-17 June, 2010; 89–94. DOI: 10.1109/pmaps.2010.5528980.
32. Boukhezzar B, Siguerdidjane H. Nonlinear control of a variable-speed wind turbine using a two-mass model. *IEEE Transactions on Energy Conversion* 2011; **26**: 149–162. DOI: 10.1109/tec.2010.2090155.
33. Østergaard KZ, Brath P, Stoustrup J. Estimation of effective wind speed. *Journal of Physics: Conference Series* 2007; **75**: 1–9. DOI: 10.1088/1742-6596/75/1/012082.
34. Bianchi F, deBattista H, Mantz RJ. *Wind Turbine Control Systems: Principles, Modelling and Gain Scheduling Design*. Springer: London, 2007.
35. Kodama N, Matsuzaka T, Inomata N. Power variation control of a wind turbine generator using probabilistic optimal control, including feed-forward control from wind speed. *Wind Engineering* 2000; **24**: 13–23. DOI: 10.1260/0309524001495378.
36. Tsui CC. *Robust Control System Design: Advanced State Space Techniques* (2nd edn). Mercel Dekker: New York, 2004.
37. Doyle J, Stein G. Robustness with observers. *IEEE Transactions on Automatic Control* 1979; **24**: 607–611. DOI: 10.1109/tac.1979.1102095.
38. Leigh JR. *Control Theory* (2nd edn). The Institution of Engineering and Technology: London, 2004.
39. Leith D, Leithead W. Implementation of wind turbine controllers. *International Journal of Control*, 1997; **66**: 349–380. DOI: 10.1080/002071797224621.
40. Ogata K. *Modern Control Engineering* (3rd edn). Prentice-Hall: Upper Saddle River, 1997.
41. Astrom KJ, Murray RM. *Feedback Systems: An Introduction for Scientists and Engineers*. Princeton University Press: Oxfordshire, 2008.